Tailoring Heterogeneous Microstructure in a High-Strength Low-Alloy Steel for Enhanced Strength-Toughness Balance

Yishuang Yu [1,2,3], Minliang Gao [1], Bin Hu [1], Chang Tian [1], Xuequan Rong [1], Zhenjia Xie [1,3], Hui Guo [1,2,3,*] and Chengjia Shang [1,2,3,*]

1 Collaborative Innovation Center of Steel Technology, University of Science and Technology Beijing, Beijing 100083, China; b20170478@xs.ustb.edu.cn (Y.Y.); g20179053@xs.ustb.edu.cn (M.G.); b20160475@xs.ustb.edu.cn (B.H.); b20170490@xs.ustb.edu.cn (C.T.); rongxuequan@tsinghua.edu.cn (X.R.); zjxie@ustb.edu.cn (Z.X.)
2 Yantai Institute of Industrial Technology, University of Science and Technology Beijing, Yantai 264003, China
3 Yangjiang Branch, Guangdong Laboratory for Materials Science and Technology (Yangjiang Advanced Alloys Laboratory), Yangjiang 529500, China
* Correspondence: guohui@mater.ustb.edu.cn (H.G.); cjshang@ustb.edu.cn (C.S.)

Abstract: The attainment of both strength and toughness is of vital importance to most structural materials, although unfortunately they are generally mutually exclusive. Here, we report that simultaneous increases in strength and toughness in a high-strength low-alloy (HSLA) steel were achieved by tailoring the heterogeneous microstructure consisting of soft intercritical ferrite and hard martensite via intercritical heat treatment. The heterogeneous microstructure features were studied from the perspective of morphology and crystallography to uncover the effect on mechanical properties. Specifically, the volume fraction of martensite increased with increasing annealing temperature, which resulted in increased back stress and effective stress, and thereby an improved strength-ductility combination. The enrichment of carbon and alloying elements in the martensite was lowered with the increase in annealing temperature. As a result, the hardness difference between the intercritical ferrite and martensite was reduced. In addition, the globular reversed austenite preferentially grew into the adjacent austenite grain that held no Kurdjumov-Sachs (K-S) orientation relationship with it, which effectively refined the coarse prior austenite grains and increased the density of high angle grain boundaries. The synergy of these two factors contributed to the improved low-temperature toughness. This work demonstrates a strategy for designing heterostructured HSLA steels with superior mechanical properties.

Keywords: high-strength low-alloy steel; intercritical heat treatment; heterogeneous microstructure; reversed austenite; yield ratio; impact toughness

1. Introduction

High-strength low-alloy (HSLA) steels are widely used for the construction of offshore platforms, bridges, buildings, and engineering machines due to their high strength, high toughness, and good weldability [1]. In general, HSLA steels are treated by quenching and tempering (Q&T) to obtain tempered martensite/bainite and nano precipitates so as to ensure an excellent combination of strength and toughness [2,3]. However, the single martensitic/bainitic structure obtained by the Q&T processing often leads to a high yield ratio, which cannot meet specific service requirements [4]. In recent years, intercritical heat treatment has proven to be an effective approach to obtain low yield ratio and balanced strength and toughness, by which a heterogeneous microstructure can be achieved through introducing a soft phase to the hard matrix [5,6].

Heterogeneous microstructure with hard and soft phases is characterized by microstructural heterogeneity and/or compositional heterogeneity, which lead to a dramatic difference in strength between different structures [4,6–8]. The strength mismatch between

different structures will cause the inhomogeneous deformation in local areas, by which a strain gradient around the interfaces could be triggered, and geometrically necessary dislocations (GNDs) could build up. In addition, stress partitioning could occur within different structures. As a result, back stress will be induced because of the generation of GNDs and the stress partitioning, which contributes to the improvement of strength and ductility [9,10]. Accordingly, numerous efforts have been made for high-strength steels with heterogeneous structures, mainly focusing on the steels containing retained austenite and aiming at the stability control of retained austenite and its influence on ductility and toughness [5,11–21]. For HSLA steels without retained austenite, the mechanical properties are affected by the features of heterogeneous microstructure, i.e., volume fraction and hardness of soft and hard phases and the microstructure refinement, showing different characteristics of mechanical behavior [4,22,23]. However, the morphological and crystallographic features of the heterogeneous microstructure without retained austenite in HSLA steels are poorly understood to date and need further investigation. In addition, the effects of heterogeneous microstructure on yield ratio and impact toughness also need to be clarified.

In this study, a low carbon low-alloy steel was used and treated by intercritical heat treatment. The morphological and crystallographic features of the heterogeneous microstructure in the steel annealed at different temperatures were characterized using scanning electron microscopy (SEM) and electron back-scattering diffraction (EBSD). This study attempts to demonstrate the effect of heterogeneous microstructure features on the strength and toughness of the low carbon low-alloy steel.

2. Materials and Methods

The chemical composition of experimental steel is $Fe - 0.09C - 0.21Si - 1.43Mn - 2.66(Cr + Ni + Cu + Mo) - 0.15(Nb + V + Ti) - 0.0010B$ (wt.%). The studied steel was melted in a vacuum induction furnace and forged into slabs with a cross section of 80 mm $\times$ 80 mm. The slabs were homogenized at 1200 °C for 2 h and then hot rolled to 12 mm through 7 passes, followed by air cooling to room temperature. The relationship between temperature and phase volume fraction of the steel was calculated using Thermo-Calc® software with TCFE7 database (Thermo-Calc Software AB, Solna, Sweden), as shown in Figure 1. The A_3 temperature, starting transformation temperature of austenite (fcc) to ferrite (bcc), is 812 °C. From 550 to 812 °C, the volume fraction of reverse austenite increased with the increase in temperature. After holding at 740, 760, 780, and 800 °C for a long time, 36%, 48%, 65%, and 85% reverse austenite was obtained, respectively.
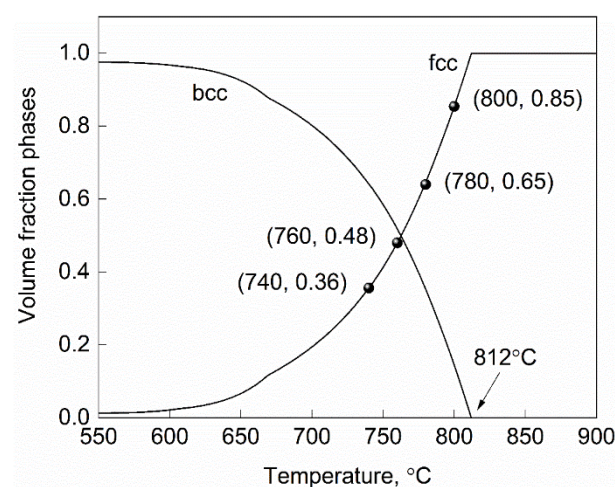

Figure 1. Temperature–volume fraction phase diagram of experimental steel; bcc and fcc stand for body-centered cubic and face-centered cubic, respectively.

The steel was first austenitized at 900 °C for 60 min and water quenched to ambient temperature. The quenched steels were then intercritically annealed at 740, 760, 780, and 800 °C for 30 min and followed by quenching in water to obtain heterogeneous microstructure, designated as IA740, IA760, IA780, and IA800, respectively. After heat treatments, tensile properties were evaluated using a universal testing machine (WDW-200, Changchun, China) with a strain rate of $1.0 \times 10^{-3} \text{ s}^{-1}$ at room temperature. The tensile samples with a diameter of 5 mm and a gauge length of 25 mm (ASTM E8) were machined parallel to the transverse direction of the heat-treated plates. The impact toughness in the transverse direction was measured using Charpy V-notch samples (ASTM E23) machined along the rolling direction. The dimensions of the samples were 10 mm in thickness, 10 mm in width, and 55 mm in length. Charpy impact tests were conducted on a pendulum impact testing machine (ZBC-450, Shanghai, China) at −40 °C, and three samples were tested for each condition.

The samples were mounted and mechanically polished using standard metallographic procedures. After being mechanically polished, the samples were etched with 3 vol.% nital solution and electropolished using a solution containing 85 vol.% ethanol, 10 vol.% perchloric acid, and 5 vol.% glycerol to obtain morphology and crystallography information, respectively. SEM observation and EBSD examination were done on a TESCAN MIRA3 field emission scanning electron microscopy (TESCAN, Brno, Czech Republic) equipped with Oxford-EBSD system (Oxford Instruments, Oxford, UK). EBSD data were obtained under the following conditions: accelerating voltage, 20 kV; working distance, 15 mm; tilt angle, 70°; step size, 80 nm. The crystallographic orientation data were post-processed with HKL Channel 5 software (Oxford Instruments, Oxford, UK), and MATLAB® software (MathWorks, Natick, MA, USA) was used to calculate the density of grain boundaries. In addition, to clarify the effect of annealing temperature on the formation of reversed austenite, the $\alpha' \rightarrow \gamma$ phase transformation was simulated by DICTRA software (Thermo-Calc Software AB, Solna, Sweden) using TCFE7 and MOB3 databases [24].

To reveal the relationship between yield ratio (*YR*) and annealing temperature, the experimental *YR* was calculated based on the Swift equation. The Swift equation shows that the *YR* of the heterogeneous microstructure can be expressed as a function of proprietary material constants [25,26]. The equation is as follows:

$$YR = \frac{\left[b + \ln(1 + e_{\mathrm{y}})\right]^N}{(1 + e_{\mathrm{y}})} \frac{\exp(N - b)}{N^N} \tag{1}$$

where e_{y} is the engineering strain at yield strength, which is set as 0.2%, and *b* and *N*, the strain constant and work hardening exponent, respectively. As the materials constants, *b* and *N* are controllable variables to determine the value of *YR*. The value of *b* is related to the constituent phases in the matrix [27], which could be estimated from the following relation:

$$b = (\alpha_{\mathrm{PF}} X_{\mathrm{PF}} + \alpha_{\mathrm{AF}} X_{\mathrm{AF}} + \alpha_{\mathrm{GB}} X_{\mathrm{GB}} + \alpha_{\mathrm{BF}} X_{\mathrm{BF}}) \exp(-k X_{\mathrm{M}}) + \alpha_{\mathrm{M}} X_{\mathrm{M}} \tag{2}$$

where α_{i} is the inherent value of each constituent phase, X_{i}, the fraction of each constituent phase, and *k* is the constant dependent on the martensite or martensite/austenite (M/A) constituent. The values of α for polygonal ferrite (PF), acicular ferrite (AF), granular bainite (GB), bainitic ferrite (BF), and martensite (M) are proposed as 0.03, 0.015, 0.008, 0.003, and 0.0003, respectively. The value of *N* is complexly associated with grain size, density of dislocations, fraction of precipitates, and concentration of alloying elements. According to the Swift equation, $N = b + \varepsilon_{\mathrm{u}}$, where ε_{u} is the true strain corresponding to the ultimate tensile strength.

3. Results

3.1. Mechanical Properties

Figure 2 and Table 1 show the mechanical properties of the steels annealed at different temperatures. It can be seen that the strength and toughness increased simultaneously with

the increase in annealing temperature, whereas the ductility decreased. With increasing annealing temperature, the yield strength increased from 645 to 823 MPa, the ultimate tensile strength increased from 1013 to 1155 MPa, and the impact energy at $-40\,°C$ increased from 43.0 to 86.0 J. The yield strength increased approximately 60 MPa for an increment of $20\,°C$ in annealing temperature, showing an approximately linear relationship with the annealing temperature. When the annealing temperature exceeded $760\,°C$, the increment of impact energy gradually decreased. In addition, the yield ratio increased as the annealing temperature increased, which is still in an appropriate range for structural applications. The steels annealed at $800\,°C$ (IA800) exhibited the best comprehensive mechanical properties, with the yield and ultimate tensile strength of 823 and 1155 MPa, respectively, the yield ratio, 0.71, the total elongation, 15.0%, and the impact energy at $-40\,°C$, 86.0 J. It is obvious that the steel shows a better combination of strength and toughness with increasing annealing temperature.
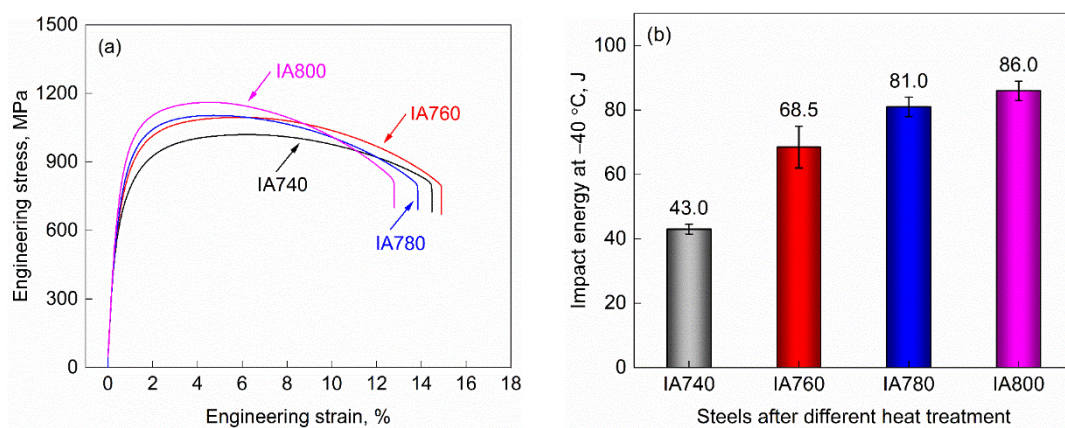

Figure 2. Mechanical properties of the steels annealed at different temperatures: (**a**) engineering stress-strain curves and (**b**) Charpy impact energy at $-40\,°C$.

Table 1. Tensile properties of the steels annealed at different temperatures.

Steel	YS [1] (MPa)	UTS [2] (MPa)	YR [3]	UEL [4] (%)	TEL [5] (%)
IA740	645	1013	0.64	6.2	16.2
IA760	708	1086	0.65	6.0	17.0
IA780	762	1099	0.69	4.7	15.2
IA800	823	1155	0.71	4.4	15.0

[1] YS is the yield strength; [2] UTS, ultimate tensile strength; [3] YR, yield ratio (YS/UTS); [4] UEL, uniform elongation; [5] TEL, total elongation.

3.2. Microstructural Characterization

3.2.1. Morphological Structures

The microstructure of the steels annealed at different temperatures characterized by SEM is depicted in Figure 3. After intercritical annealing, a heterogeneous microstructure of intercritical ferrite and martensite was obtained. The martensite can be classified into granular martensite and fibrous martensite according to its morphology, which was derived from the different reversed austenite. When annealed at the ($\alpha + \gamma$) region, globular reversed austenite is formed at the prior austenite grain boundaries as well as martensite packet and block boundaries, and acicular reversed austenite is formed at martensite packet, block, or lath boundaries [28]. These two types of reversed austenite would be transformed to granular martensite and fibrous martensite during the cooling process, respectively. The fraction of those newly formed martensite increased with increasing annealing temperature. The microstructure of IA740 and IA760 steels was dominated by intercritical ferrite, whereas the leading microstructure in IA780 and IA800 steels was newly formed martensite.
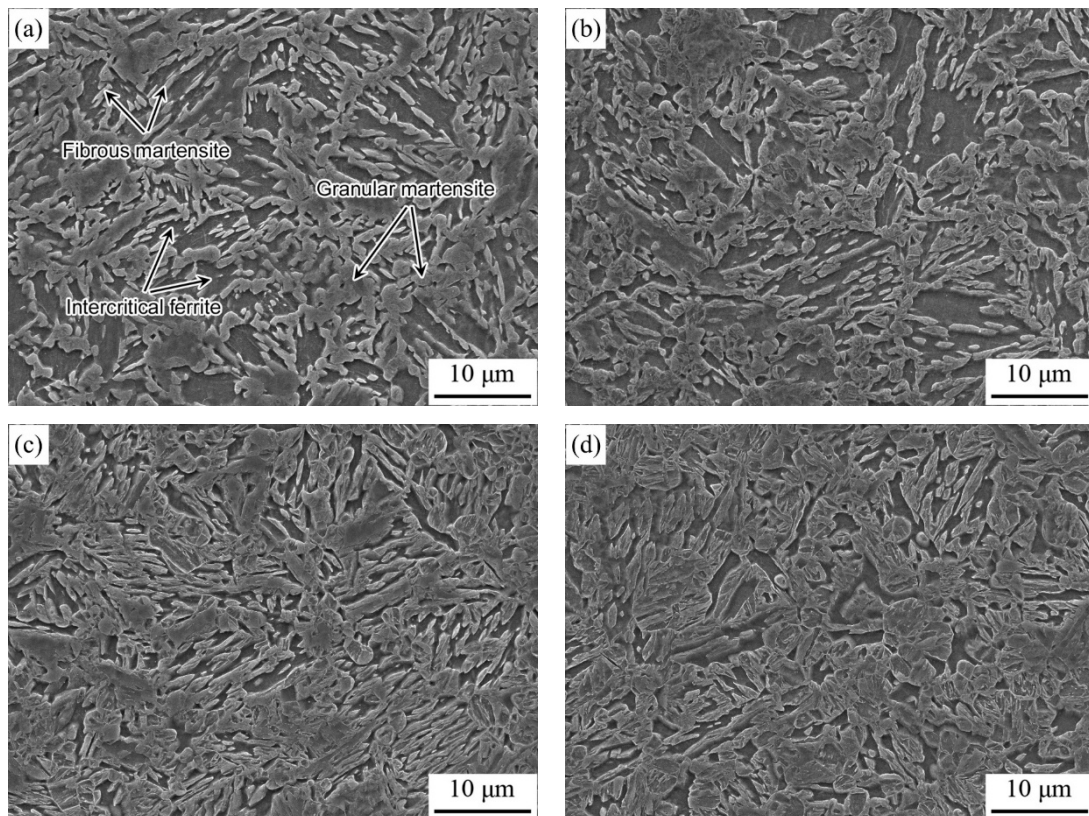
Figure 3. SEM micrographs of the steels annealed at different temperatures: (**a**) IA740, (**b**) IA760, (**c**) IA780, and (**d**) IA800.

3.2.2. Crystallographic Features

Figure 4 shows the band contrast (BC) maps depicting the microstructure morphology of the steels annealed at different temperatures. Obviously, the heterogeneous microstructure of the steels consisted of intercritical ferrite and martensite (bcc). No retained austenite (fcc) was observed. In IA740 steel, many fine globular particles with size of approximately 1.5 μm can be seen. These particles were martensite transformed from the globular reversed austenite during cooling, and they were mainly distributed at the boundaries of prior austenite grains, martensite packets and blocks. Moreover, there existed grains with size of approximately 15 μm in IA740 steel, which is similar to the prior austenite grain size in the microstructure quenched from 900 °C. As the annealing temperature increased from 740 to 800 °C, the globular reversed austenite grew up gradually and grew into one of the two adjacent austenite grains. In IA780 and IA800 steels, the size of globular reversed austenite was approximately 2 μm, and the microstructure was much finer than that in the steels annealed at 740 and 760 °C.

Band contrast maps showing the boundary distribution of the steels annealed at different temperatures are depicted in Figure 5. The boundaries were divided into three types according to the misorientation (θ) and highlighted by lines with different colors, i.e., white ($5° < \theta < 15°$), black ($15° < \theta < 45°$), and yellow ($\theta > 45°$). It was found that the interfaces of globular reversed austenite were high angle grain boundaries (HAGBs) with misorientation between 15° and 45°, and the HAGBs with misorientation greater than 45° were dominant inside the globular reversed austenite grains. The size of globular reversed austenite grains gradually increased with an increase in annealing temperature, resulting in a significant increase in density of HAGBs ($\theta > 15°$). The steels annealed at higher temperatures (780 and 800 °C) exhibited higher density of HAGBs ($\theta > 15°$) than the steels annealed at lower temperatures (740 and 760 °C). Clearly, the globular reversed austenite grew significantly when annealed at higher temperatures, which is beneficial to the refinement of the coarse prior austenite grains.
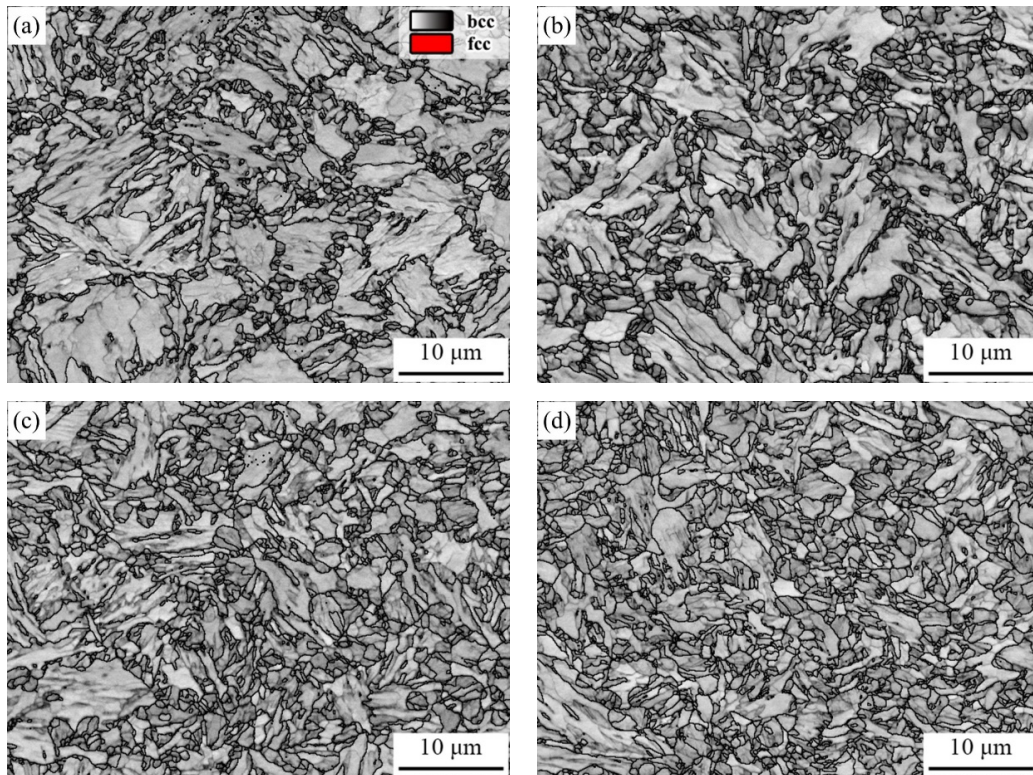
Figure 4. Band contrast (BC) maps depicting the microstructure morphology of the steels annealed at different temperatures: (**a**) IA740, (**b**) IA760, (**c**) IA780, and (**d**) IA800. No retained austenite (fcc) was observed, and black lines denote high angle grain boundaries.
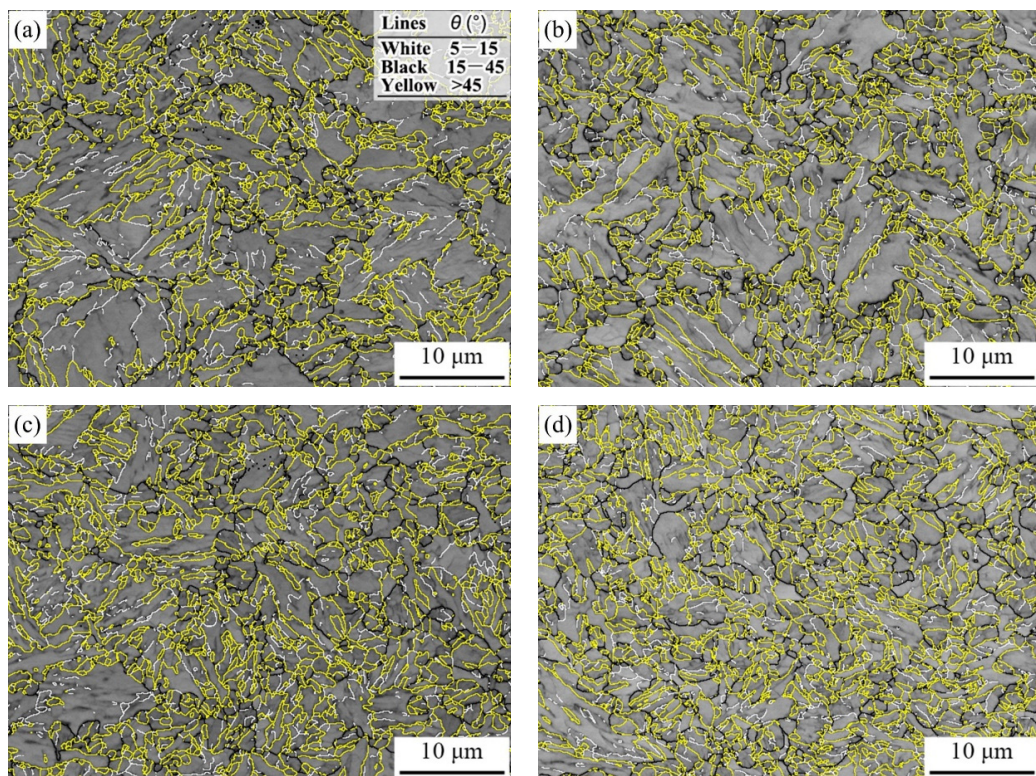

Figure 5. Band contrast (BC) maps showing the boundary distribution of the steels annealed at different temperatures: (**a**) IA740, (**b**) IA760, (**c**) IA780, and (**d**) IA800.

The Kernel average misorientation (KAM) maps of the steels annealed at different temperatures are shown in Figure 6. The KAM can represent the density distribution of local dislocations that are related to geometrically necessary dislocations [29]. Thus, the change in dislocation density of the steels can be revealed by KAM distribution. In IA740 steel, a remarkable KAM variation was observed in the granular martensite, fibrous martensite, and intercritical ferrite. It is obvious that the granular martensite exhibited high KAM values. The areas with high KAM values inside the large grains were fibrous martensite, whereas the areas with low KAM values were intercritical ferrite. This indicates that the dislocations are heterogeneously distributed in the microstructure. With the increase in annealing temperature, the areas with high KAM values increased gradually. Compared with IA740 and IA760 steels, the areas with high KAM values in IA780 and IA800 steels were larger and the distribution of KAM values was more uniform.
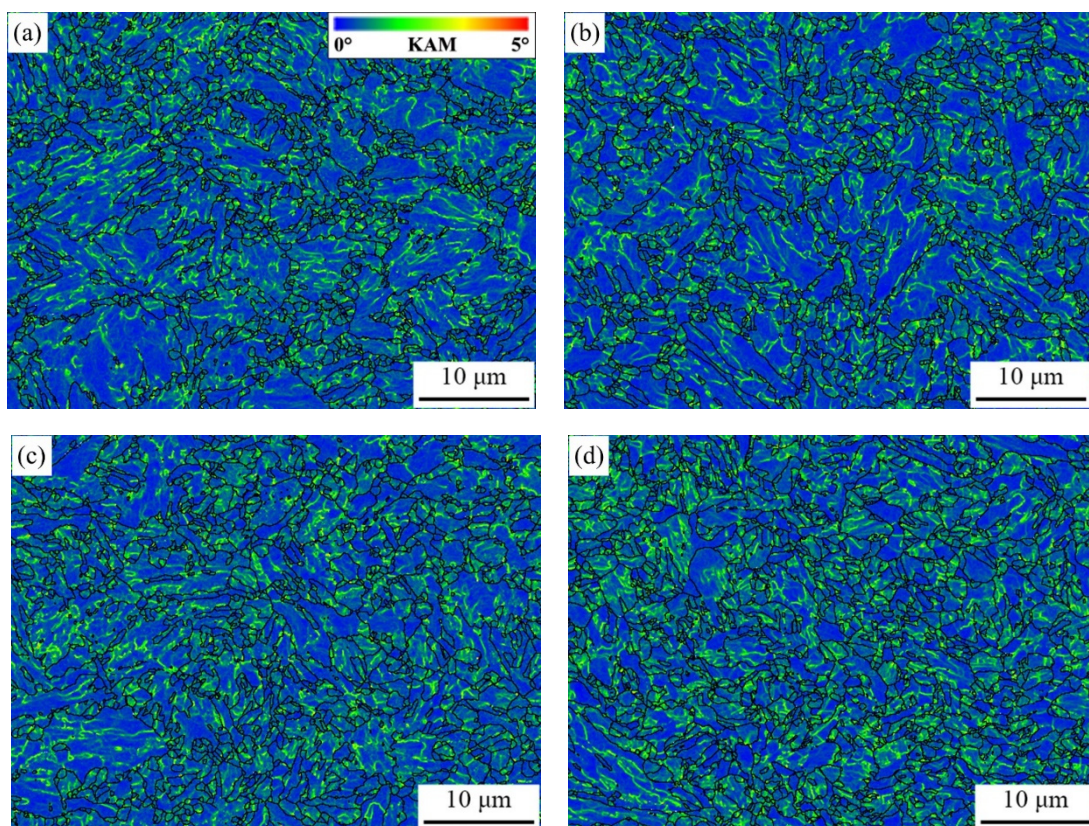

Figure 6. Kernel average misorientation (KAM) maps of the steels annealed at different temperatures: (**a**) IA740, (**b**) IA760, (**c**) IA780, and (**d**) IA800. Black lines denote high angle grain boundaries.

4. Discussion

4.1. Microstructure Analysis

#### 4.1.1. Features of Constituent Phase in Heterogeneous Microstructure

The volume fraction of each phase in the steels annealed at different temperatures is summarized in Table 2. Ten SEM micrographs were counted and analyzed to obtain the volume fraction of intercritical ferrite and martensite by point counting, and the volume fraction of reversed austenite was predicted by Thermo-Calc software. It was found that the volume fraction of martensite in the matrix was close to the predicted reversed austenite fraction. With increasing annealing temperature, the volume fraction of martensite increased gradually. In IA740 and IA760 steels, the matrix was mainly composed of intercritical ferrite with volume fraction of 63.5% and 51.0%, respectively. On the contrary, the matrix in IA780 and IA800 steels was dominated by martensite, the volume fraction of which was 65.8% and 86.0%, respectively.

Table 2. Volume fraction of each constituent phase of the steels annealed at different temperatures (vol.%).

Steel	f_{IF} [1]	f_M [2]	f_{RA} [3]
IA740	63.5 ± 2.0	36.5 ± 2.0	35.7
IA760	51.0 ± 1.1	49.0 ± 1.1	48.1
IA780	34.2 ± 1.2	65.8 ± 1.2	64.7
IA800	14.0 ± 1.4	86.0 ± 1.4	85.4

[1] f_{IF}, volume fraction of intercritical ferrite; [2] f_M, volume fraction of martensite; [3] f_{RA} is the volume fraction of reversed austenite. The f_{RA} was calculated by Thermo-Calc software, others were measured by point counting.

Figure 7 shows the KAM distribution of the steels annealed at different temperatures. It is noted that the KAM value of the steels was mainly distributed in a range of 0–2.0° and the peak fraction of KAM value appears near 0.5° (Figure 7a). The distribution peak of KAM values became lower as the annealing temperature increased, and the fraction of KAM value in the range of 0.5–1.5° became higher (Figure 7b). This suggested that the dislocation density in the matrix was increased with annealing temperature and the distribution was more uniform in the steels annealed at higher temperatures.
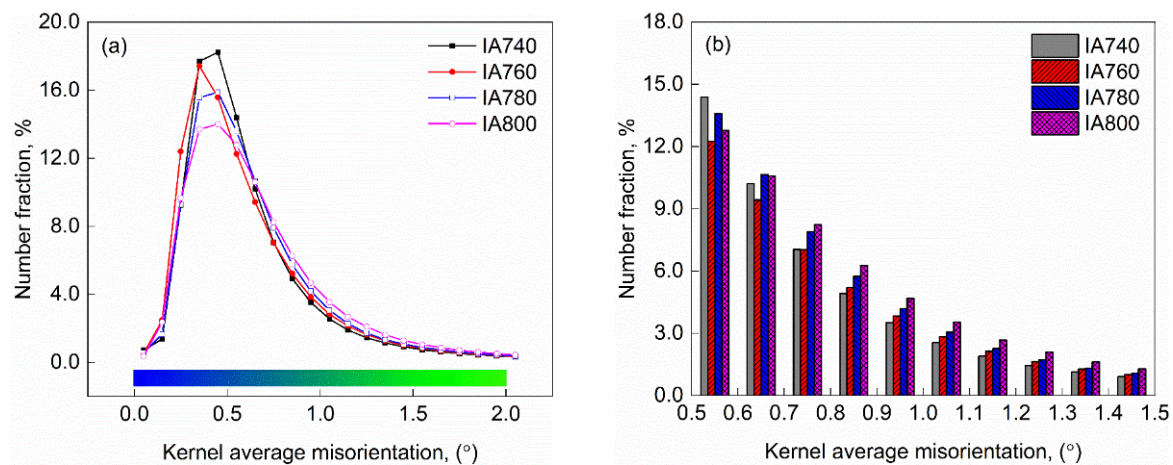
Figure 7. KAM distribution in ranges of 0–2.0° (**a**) and 0.5–1.5° (**b**) of the steels annealed at different temperatures.

4.1.2. Formation of Reversed Austenite

The $\alpha' \rightarrow \gamma$ transformation was simulated by DICTRA software, which assumes local equilibrium at the α'/γ (bcc/fcc) interface. The initial condition of DICTRA simulation is shown in Figure 8a, which ignored the nucleation progress. The growth morphology was assumed to be planar and the width of martensite lath (bcc) was set to be 500 nm based on SEM micrographs. The thickness of initial austenite (fcc) was assumed to be 1 nm. To simplify the simulation, Fe, C, Si, Mn, and Ni were considered for the simulation, and the initial composition of bcc and fcc phases was set as Fe-0.09C-0.21Si-1.43Mn-1.05Ni (wt.%). The transformation during isothermal annealing at 740, 760, 780, and 800 °C for 30 min was simulated. Figure 8b depicts the carbon concentration profiles in bcc and fcc phases. The carbon atoms were enriched in the reversed austenite (fcc) during annealing. Due to the rapid diffusion of carbon in the annealing temperature range, carbon was uniformly distributed in the fcc or bcc phases and no carbon gradient was observed. With the increase in annealing temperature, the size of reversed austenite increased and the enrichment of carbon in the reversed austenite decreased. Figure 8c,d shows the variation of Mn and Ni concentration distribution with annealing temperature, respectively. The Mn and Ni exhibited concentration gradient in the reversed austenite owing to the slow diffusion of Mn and Ni in the fcc phase at the annealing temperature. In addition, the enrichment of Mn and Ni in the reversed austenite decreased as the annealing temperature increased. Clearly, the heterogeneous microstructure was composed of the lean alloyed intercritical ferrite and

alloy-enriched martensite. Because hardness is mainly related to the content of carbon and alloying elements in the matrix [30], the variation of element enrichment in the reversed austenite will affect the hardness difference between the intercritical ferrite and martensite in the heterogeneous structure. It is concluded that the hardness difference between the intercritical ferrite and martensite would be decreased as the element enrichment in the reversed austenite decreased with annealing temperature.
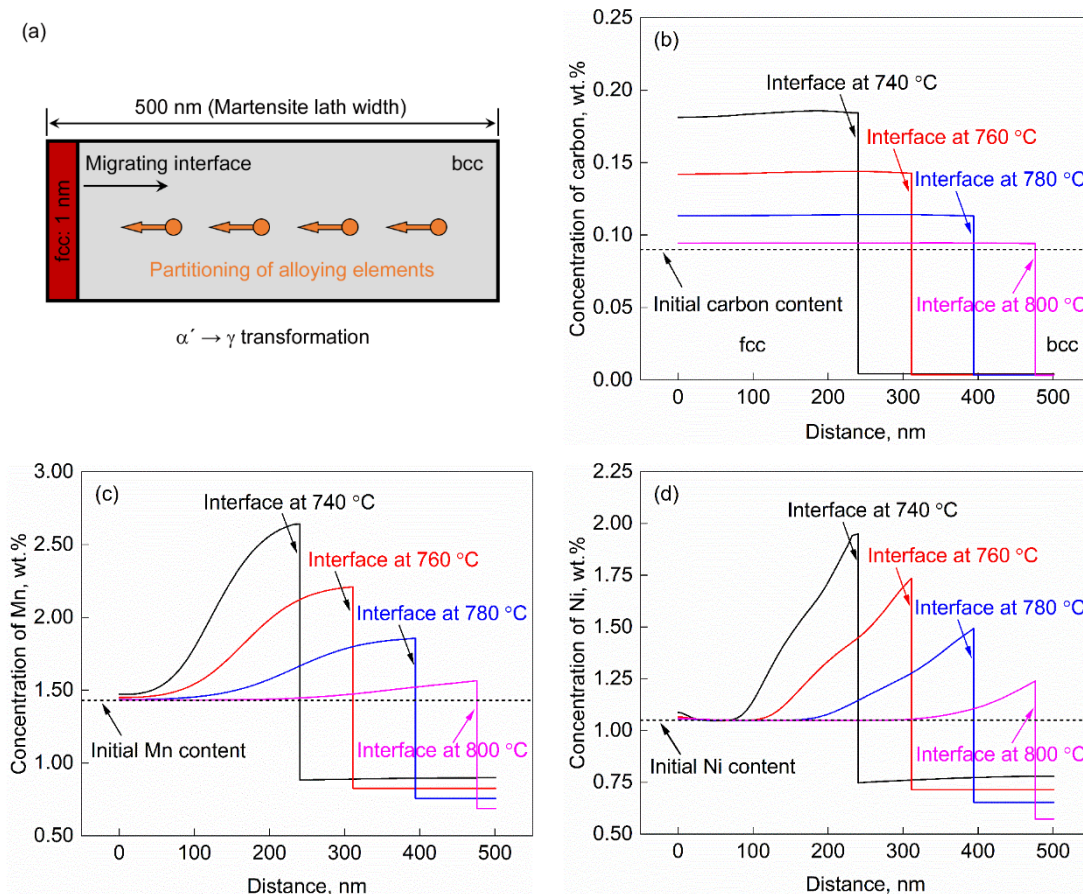

Figure 8. Partitioning of elements in the steels annealed at different temperatures: (**a**) initial condition of DICTRA simulation, (**b**) carbon concentration profiles, (**c**) Mn concentration profiles, and (**d**) Ni concentration profiles.

The results of the DICTRA simulation showing the transformation kinetics of reversed austenite during the $\alpha' \rightarrow \gamma$ transformation are depicted in Figure 9. Two inflection points were marked by points A and B in the reversed austenite growth curve, which indicate the transitions of the diffusion-controlled mechanism. The reversed austenite growth in the $\alpha' \rightarrow \gamma$ transformation consists of three stages [31]: initial negligible-partitioning growth controlled by rapid carbon diffusion in ferrite, which is gradually replaced by carbon diffusion in austenite (before point A); intermediate slow growth controlled by diffusion of Mn and other substitutional elements in ferrite (between points A and B); and very slow growth controlled by diffusion of substitutional elements in austenite for final equilibration, which may cause the shrinkage of austenite (after point B). With the increase in annealing temperature, the diffusion rate of carbon and alloying elements increased, and the transformation rate increased. As a result, the time interval to reach points A and B was shortened with increasing annealing temperature, and the volume fraction of reversed austenite was increased.
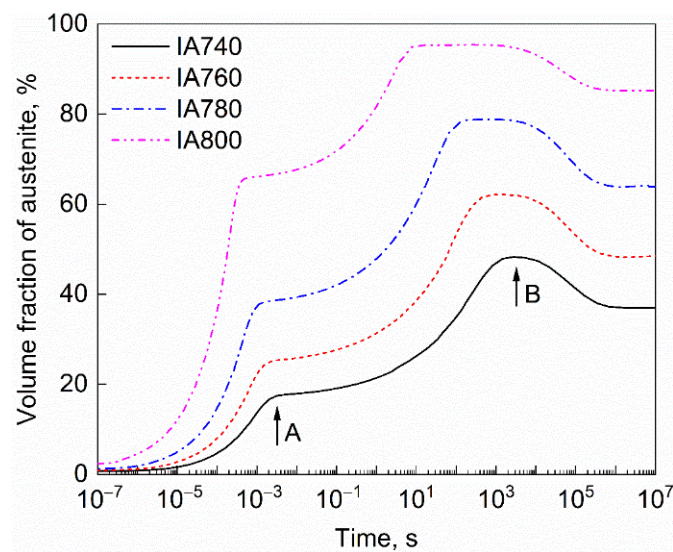
Figure 9. Transformation kinetics of reversed austenite in the steels annealed at different temperatures.

4.1.3. Crystallographic Characteristics of Heterogeneous Microstructure

Figure 10 shows the density of grain boundaries in the steels annealed at different temperatures. It can be seen that the density of HAGBs ($\theta > 15°$) increased gradually with increasing annealing temperature. The variation in the density of HAGBs ($15° < \theta < 45°$) indicates that the prior austenite grains are refined gradually as the annealing temperature increased. The increase in the density of HAGBs ($\theta > 15°$) is mainly associated with the formation of globular reversed austenite.
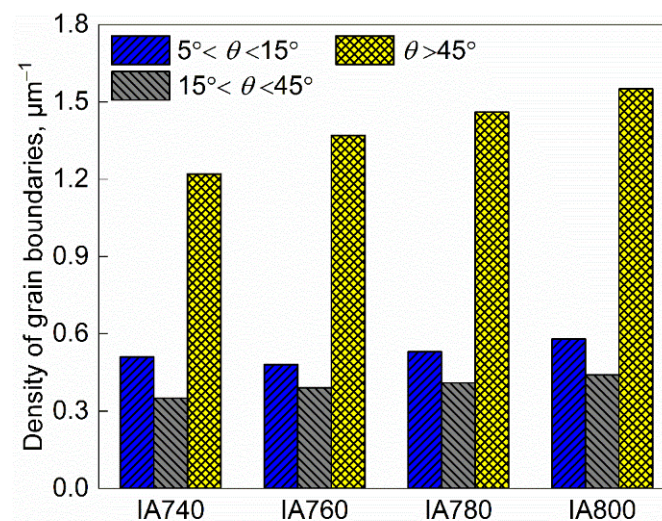

Figure 10. Boundary density of the steels annealed at different temperatures.

The crystallographic characteristics of heterogeneous microstructure are presented in Figure 11. Figure 11a,b shows the BC map and inverse pole figure (IPF) of the typical heterogeneous structure, respectively, in which four selected prior austenite grains (PAGs) are highlighted. The γ_C and γ_D grains were located between the γ_A and γ_B, which were globular reversed austenite formed during annealing. In addition, the dark gray acicular structures inside the γ_A and γ_B grains were fibrous martensite transformed from acicular reversed austenite. Figure 11c–f shows the $\{001\}_{bcc}$ pole figures corresponding to the γ_A, γ_B, γ_C, and γ_D, respectively. Because the martensite holds near K-S OR with the prior austenite grain, the $\{001\}_{bcc}$ pole figure of matrix shows a characteristic K-S pattern. The orientations of the granular martensite transformed from the γ_C (γ_D) well matched with

the K-S pattern of the γ_B (γ_A) grain, whereas it deviated largely from those in the γ_A (γ_B) grain. This indicates that the γ_C (γ_D) has an almost identical orientation with the γ_B (γ_A) grain. In addition, the γ_C (γ_D) grain grew into γ_A (γ_B) grain. It is concluded that the globular reversed austenite preferentially grew into the adjacent austenite grain that held no K-S orientation relationship with it, which can effectively refine the coarse prior austenite grains [32,33]. Clearly, with the increase in annealing temperature, the size of globular reversed austenite increased and thus the density of HAGBs increased.
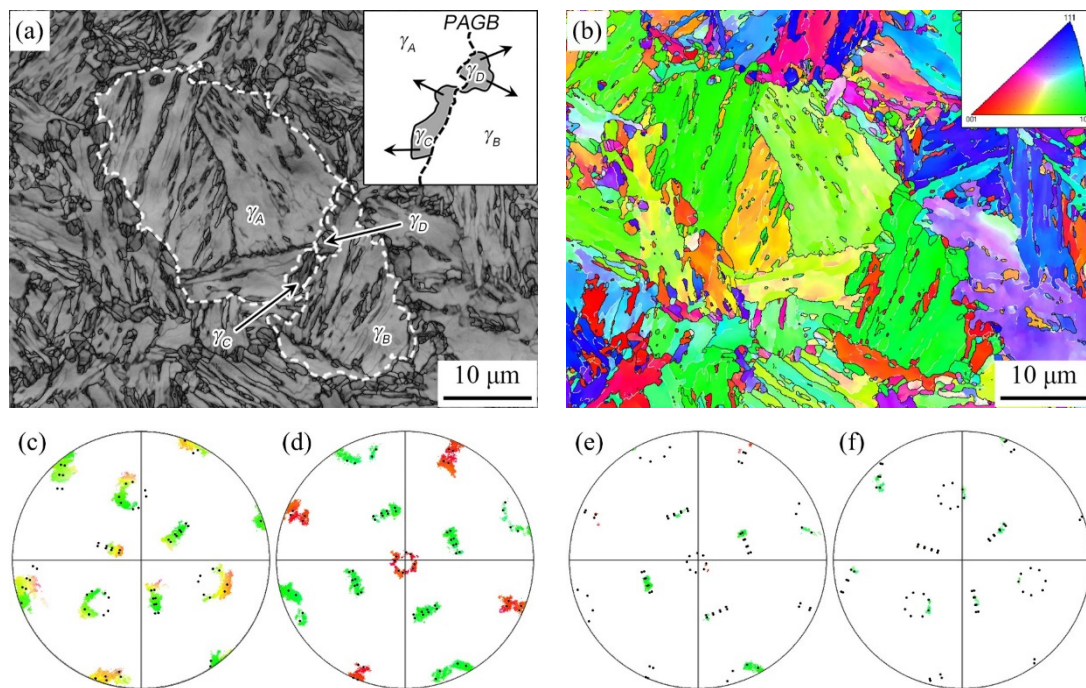

Figure 11. Crystallographic characteristics of heterogeneous microstructure: (**a**) BC map highlighting the selected prior austenite grains (PAGs) and schematic illustration showing the growth of globular reversed austenite into one side of the PAG, (**b**) inverse pole figure (IPF) showing the orientation of PAGs, and (**c–f**) {001}$_{bcc}$ pole figures corresponding to the γ_A, γ_B, γ_C, and γ_D in image (**a**), respectively. White and black lines in image (**b**) represent low (5–15°) and high (>15°) angle grain boundaries, respectively.

4.2. Analysis of Mechanical Behavior

4.2.1. Strength and Work Hardening Behavior

To reveal the strength variation and work hardening behavior of heterogeneous microstructure, the extended Kocks–Mecking (K–M) curves of the steels were analyzed, as shown in Figure 12. The extended K–M curve shows the relationship between the work hardening rate (dσ/dε) and the true stress. Before reaching the tensile strength, the change of the work hardening rate can be divided into two stages, separated by the yield point [34]. The first stage is an elastic deformation stage caused by the anelastic reversible behavior for the bowing of matrix dislocations (Stage I), and the second stage is a plastic deformation stage associated with the effective accumulation of dislocations (Stage II). It is found that the steels annealed at different temperatures showed continuous yielding behavior and high initial work hardening rate. The deformation behavior of the steels at initial stage is associated with the residual stress and geometrically necessary dislocations (GNDs) in the intercritical ferrite. The residual stresses are considered to be responsible for lowering the yield strength, whereas the unpinned GNDs contribute to the continuous initial yielding [35]. As a result, a rapid work hardening at the early stage of deformation was observed. With the increase in annealing temperature, the ultimate tensile strength and work hardening rate at each stress increased, which were mainly related to the volume fraction of martensite. It has been shown that the work hardening rate of the steels with

heterogeneous microstructure is related to $\sqrt{V_M/D_M}$ [36], where V_M is the volume fraction of martensite and D_M is the average diameter of martensite islands. At a given D_M, the work hardening capability will be enhanced by increasing the V_M. In this study, the volume fraction of martensite increased significantly with increasing annealing temperature, but the size was almost the same, thus the work hardening rate increased.
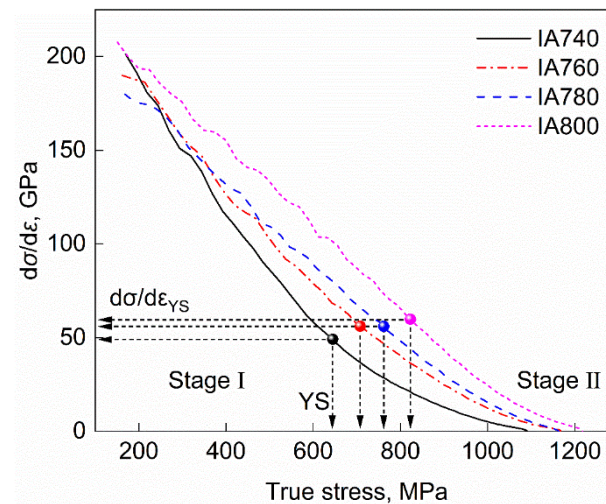

Figure 12. Extended K–M curves of the steels annealed at different temperatures. The transition marked by black, red, blue, and magenta dots representing the yield strength (YS) of IA740, IA760, IA780, and IA800, respectively.

With the increase in annealing temperature, the fraction of martensite in the matrix gradually increased, and the combination of strength and ductility was significantly improved, which is related to the simultaneous enhancement of back stress and effective stress [7]. The back stress originates from the stress partitioning due to the strength mismatch between intercritical ferrite and martensite [22,37], and the deformation heterogeneity will be enhanced with the increase in martensite fraction in the matrix. Accordingly, the steels with higher martensite fraction (IA780 and IA800) showed higher back stress. The effective stress is closely related to the forest hardening in intercritical ferrite [7]. The plastic strain will be more concentrated in the intercritical ferrite during the tensile test, and more dislocations are thus generated in this microconstituent. These high-density dislocations will bring significant dislocation forest hardening and improve the effective stress. It is clear that the increase in martensite fraction in the matrix can enhance the back stress and effective stress simultaneously and improve the balance of strength and ductility.

4.2.2. Yield Ratio

It was reported that the yield ratio is approximately proportional to $ln(b/N^2)$ by simplifying Equation (1) [26]. Figure 13 shows the experimental yield ratio and estimated $ln(b/N^2)$ value of the steels annealed at different temperatures. The yield ratio can be effectively lowered by creating heterogeneous microstructure through introducing intercritical ferrite to a single martensite microstructure [4,27]. Thus, the steels annealed at different temperatures exhibited low yield ratio. In addition, the fraction of martensite increased with increasing annealing temperature. As a result, the b value increased and the N value decreased, resulting in the increase in the $ln(b/N^2)$ value and yield ratio. It can be inferred that the reduction of the yield ratio can be achieved through modifying the fraction of martensite in the heterogeneous microstructure by decreasing the value of b or increasing the value of N.
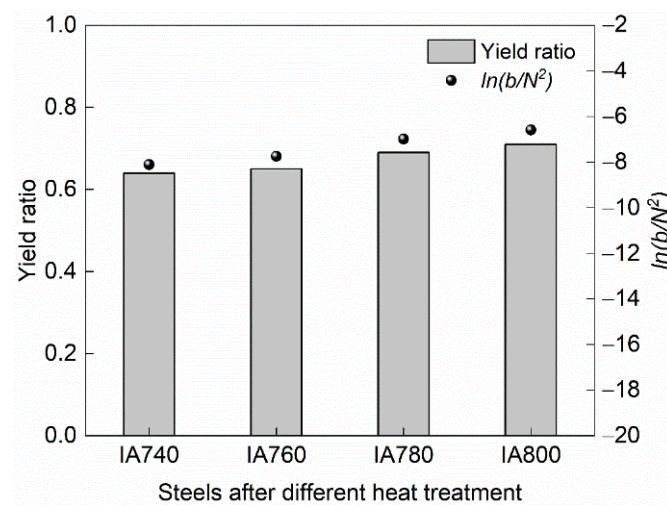
Figure 13. Experimental yield ratio and estimated value of $ln(b/N^2)$ of the steels annealed at different temperatures.

4.2.3. Toughening Mechanism

As previously noted, the $-40\ ^\circ$C impact toughness of the steels increased gradually as the annealing temperature increased. When the steel was annealed at 740 $^\circ$C, the reversed austenite of 36.5 vol.% was obtained. The reversed austenite was rich in carbon and alloying elements and transformed to martensite with high hardness during cooling [4]. The hard and brittle martensite can provide nucleation sites for cleavage cracks and deteriorate the toughness [38,39]. Therefore, the impact toughness of IA740 steel was only 43.0 J. As the annealing temperature increased to 760 $^\circ$C, the volume fraction of reversed austenite reached 49.0% whilst the enrichment of carbon and alloying elements decreased, resulting in the reduced hardness difference between soft intercritical ferrite and hard martensite. Compared with IA740 steel, the carbon and alloying element content of the martensite in IA760 steel decreased, and the density of HAGBs in the matrix was increased significantly. The reduction of hardness difference between soft intercritical ferrite and hard martensite can lower the probability of microcrack initiation [38], and the increase in density of HAGBs can effectively improve the resistance of microcrack propagation and hinder the propagation of microcrack [40]. Thus, the impact toughness of IA760 steel was enhanced. When the steel was annealed at 780 $^\circ$C, the matrix was mainly composed of martensite, and the volume fraction of martensite was approximately 65.8%. Because the content of carbon and alloying elements in martensite was further reduced and the density of HAGBs was increased, the impact toughness of IA780 steel was increased. In IA800 steel, the volume fraction of martensite in the matrix increased to 86.0%. The content of carbon and alloying elements in martensite decreased further and the density of HAGBs increased. Consequently, the impact toughness reached 86.0 J.

According to this analysis, the variation of impact toughness of the steels annealed at different temperatures is closely related to the microstructure evolution. As the annealing temperature increased, the volume fraction of reversed austenite increased and the enrichment of carbon and alloying elements decreased, which reduced the hardness difference between soft intercritical ferrite and hard martensite and the probability of microcrack initiation. Additionally, the globular reversed austenite grew up gradually with annealing temperature, which increased the density of HAGBs and the resistance of microcrack propagation. The two factors are the essential reasons for the improvement of impact toughness with increasing annealing temperature.

5. Conclusions

In this study, HSLA steel with heterogeneous microstructure was obtained by inter-critical heat treatment. The morphological and crystallographic features of the hetero-

geneous microstructure were characterized to demonstrate the effect of heterogeneous microstructure features on the strength and toughness of the HSLA steel, and the following conclusions are drawn.

(1) Heterogeneous microstructure was achieved through intercritical heat treatment in the HSLA steel that possessed comprehensive mechanical properties. With increased annealing temperature, the strength-toughness combination of the steel increased. After annealing at 800 °C, a high yield strength of 823 MPa, tensile strength of 1155 MPa, and total elongation of 15.0% were obtained. It also exhibited a −40 °C impact toughness of 86.0 J and a low yield ratio of 0.71.

(2) The heterogeneous microstructure consisted of lean alloyed intercritical ferrite and alloy-enriched martensite. The martensite can be divided into granular martensite and fibrous martensite according to its morphology, which transformed from the globular and acicular reversed austenite formed during annealing, respectively. The volume fraction of martensite increased gradually with increasing annealing temperature. In addition, the dislocations were heterogeneously distributed in the microstructure.

(3) The increase in high angle grain boundaries (HAGBs) was attributed to the formation of globular reversed austenite. The globular reversed austenite preferentially grew into the adjacent austenite grain that held no K-S orientation relationship with it, thus effectively refining the coarse prior austenite grains. The size of globular reversed austenite and density of HAGBs increased with annealing temperature.

(4) The steels annealed at different temperatures showed continuous yielding behavior. With the increase in annealing temperature, the ultimate tensile strength and work hardening rate increased, which were mainly related to the volume fraction of martensite. The increase in martensite volume fraction can enhance the back stress and effective stress simultaneously and improve the strength-ductility combination.

(5) As the annealing temperature increased, the enrichment of carbon and alloying elements in the martensite was decreased, resulting in a reduced hardness difference between soft intercritical ferrite and hard martensite. Additionally, the globular reversed austenite grew up with annealing temperature, which increased the density of HAGBs. These two factors were the underlying reasons for the improvement of impact toughness with annealing temperature.

Data Availability Statement: Data is contained within the article.

References

1. Weng, Y.Q.; Yang, C.F.; Shang, C.J. State-Of-The-Art and development trends of HSLA steels in China. *Iron Steel* **2011**, *46*, 1–10. [CrossRef]
2. Dhua, S.K.; Ray, A.; Sarma, D.S. Effect of tempering temperatures on the mechanical properties and microstructures of HSLA-100 type copper-bearing steels. *Mater. Sci. Eng. A* **2001**, *318*, 197–210. [CrossRef]
3. Xie, Z.J.; Fang, Y.P.; Han, G.; Guo, H.; Misra, R.D.K.; Shang, C.J. Structure–Property relationship in a 960 MPa grade ultrahigh strength low carbon niobium–vanadium microalloyed steel: The significance of high frequency induction tempering. *Mater. Sci. Eng. A* **2014**, *618*, 112–117. [CrossRef]
4. Yu, Y.; Hu, B.; Gao, M.; Xie, Z.; Rong, X.; Han, G.; Guo, H.; Shang, C. Determining role of heterogeneous microstructure in lowering yield ratio and enhancing impact toughness in high-strength low-alloy steel. *Int. J. Miner. Metall. Mater.* **2021**, *28*, 816–825. [CrossRef]

5. Xie, Z.; Shang, C.; Zhou, W.; Wu, B. Effect of retained austenite on ductility and toughness of a low alloyed multiphase steel. *Acta Metall. Sin.* **2016**, *52*, 224–232. [CrossRef]

6. Xie, Z.J.; Shang, C.J.; Wang, X.L.; Wang, X.M.; Han, G.; Misra, R.D.K. Recent progress in third-generation low alloy steels developed under M^3 microstructure control. *Int. J. Miner. Metall. Mater.* **2020**, *27*, 1–9. [CrossRef]

7. Gao, B.; Chen, X.; Pan, Z.; Li, J.; Ma, Y.; Cao, Y.; Liu, M.; Lai, Q.; Xiao, L.; Zhou, H. A high-strength heterogeneous structural dual-phase steel. *J. Mater. Sci.* **2019**, *54*, 12898–12910. [CrossRef]

8. Cai, Y.; Li, X.; Xia, H.; Cui, Y.; Manladan, S.M.; Zhu, L.; Shan, M.; Sun, D.; Wang, T.; Lv, X.; et al. Fabrication of laminated high entropy alloys using differences in laser melting deposition characteristics of FeCoCrNi and FeCoCrNiAl. *J. Manuf. Process.* **2021**, *72*, 294–308. [CrossRef]

9. Wu, X.; Zhu, Y. Heterogeneous materials: A new class of materials with unprecedented mechanical properties. *Mater. Res. Lett.* **2017**, *5*, 527–532. [CrossRef]

10. Wu, X.; Zhu, Y. *Heterostructured Materials: Novel Materials with Unprecedented Mechanical Properties*, 1st ed.; Jenny Stanford Publishing: New York, NY, USA, 2021; pp. 17–31.

11. Liu, S.; Xiong, Z.; Guo, H.; Shang, C.; Misra, R.D.K. The significance of multi-step partitioning: Processing-structure-property relationship in governing high strength-high ductility combination in medium-manganese steels. *Acta Mater.* **2017**, *124*, 159–172. [CrossRef]

12. Li, Y.; Lu, Y.; Li, W.; Khedr, M.; Liu, H.; Jin, X. Hierarchical microstructure design of a bimodal grained twinning-induced plasticity steel with excellent cryogenic mechanical properties. *Acta Mater.* **2018**, *158*, 79–94. [CrossRef]

13. Xie, Z.J.; Han, G.; Yu, Y.S.; Shang, C.J.; Misra, R.D.K. The determining role of intercritical annealing condition on retained austenite and mechanical properties of a low carbon steel: Experimental and theoretical analysis. *Mater. Charact.* **2019**, *153*, 208–214. [CrossRef]

14. Wan, X.; Hu, F.; Cheng, L.; Huang, G.; Zhang, G.; Wu, K. Influence of two-step bainite transformation on toughness in medium-carbon micro/nano-structured steel. *Acta Metall. Sin.* **2019**, *55*, 1503–1511. [CrossRef]

15. Han, G.; Hu, B.; Yu, Y.S.; Rong, X.Q.; Xie, Z.J.; Misra, R.D.K.; Wang, X.M.; Shang, C.J. Atomic-Scale study on the mechanism of formation of reverted austenite and the behavior of Mo in a low carbon low alloy system. *Mater. Charact.* **2020**, *163*, 110269. [CrossRef]

16. Chen, G.; Hu, H.; Xu, G.; Tian, J.; Wan, X.; Wang, X. Optimizing microstructure and property by ausforming in a medium-carbon bainitic steel. *ISIJ Int.* **2020**, *60*, 2007–2014. [CrossRef]

17. Hu, B.; Rong, X.; Tian, C.; Yu, Y.; Guo, H.; Misra, R.D.K.; Shang, C. Nanoscale precipitation and ultrafine retained austenite induced high strength-ductility combination in a newly designed low carbon Cu-bearing medium-Mn steel. *Mater. Sci. Eng. A* **2021**, *822*, 141685. [CrossRef]

18. Liu, S.; Hu, B.; Li, W.; Misra, R.D.K.; Jin, X. Refined heterogeneous phase unit enhances ductility in quenched ultra-high strength steels. *Scripta Mater.* **2021**, *194*, 113636. [CrossRef]

19. Liu, S.; Hu, B.; Yu, Y.; Shang, C.; Misra, R.D.K.; Jin, X. Shaping mechanism of ultrafine metastable austenite in HSLA steels through a cumulative process of hot rolling, partitioning and tempering. *Mater. Sci. Eng. A* **2021**, *811*, 141060. [CrossRef]

20. Wei, L.J.; Ji, X.M.; Yu, Y.S.; Misra, R.D.K.; Liu, P.C.; Wang, X.M. Retained austenite-induced fire-resistance of a 690 MPa high strength steel. *Mater. Lett.* **2021**, *291*, 129448. [CrossRef]

21. Hernandez-Duran, E.I.; Bliznuk, V.; Ros-Yanez, T.; Iquilio-Abarzua, R.; Castro-Cerda, F.M.; Petrov, R.H. Improvement of the strength-ductility balance in ultrafast heated steels by combining high-temperature annealing and quenching and partitioning process. *Mater. Sci. Eng. A* **2021**, *827*, 142045. [CrossRef]

22. Lai, Q.; Brassart, L.; Bouaziz, O.; Gouné, M.; Verdier, M.; Parry, G.; Perlade, A.; Bréchet, Y.; Pardoen, T. Influence of martensite volume fraction and hardness on the plastic behavior of dual-phase steels: Experiments and micromechanical modeling. *Int. J. Plast.* **2016**, *80*, 187–203. [CrossRef]

23. Li, X.; Sun, M.; Zhao, J.; Wang, X.; Shang, C. Quantitative crystallographic characterization of boundaries in ferrite-bainite/martensite dual-phase steels. *Acta Metall. Sin.* **2020**, *56*, 653–660. [CrossRef]

24. Andersson, J.O.; Helander, T.; Höglund, L.; Shi, P.; Sundman, B. Thermo-Calc & DICTRA, computational tools for materials science. *Calphad* **2002**, *26*, 273–312. [CrossRef]

25. Swift, H.W. Plastic instability under plane stress. *J. Mech. Phys. Solids* **1952**, *1*, 1–18. [CrossRef]

26. Kim, S.K.; Kim, Y.M.; Lim, Y.J.; Kim, N.J. Relationship between yield ratio and the material constants of the Swift equation. *Met. Mater. Int.* **2006**, *12*, 131–135. [CrossRef]

27. Kim, Y.M.; Kim, S.K.; Kim, N.J. Simple method for tailoring the optimum microstructures of high-strength low-alloyed steels by the use of constitutive equation. *Mater. Sci. Eng. A* **2019**, *743*, 138–147. [CrossRef]

28. Zhang, X.; Miyamoto, G.; Toji, Y.; Nambu, S.; Koseki, T.; Furuhara, T. Orientation of austenite reverted from martensite in Fe-2Mn-1.5Si-0.3C alloy. *Acta Mater.* **2018**, *144*, 601–612. [CrossRef]

29. Calcagnotto, M.; Ponge, D.; Demir, E.; Raabe, D. Orientation gradients and geometrically necessary dislocations in ultrafine grained dual-phase steels studied by 2D and 3D EBSD. *Mater. Sci. Eng. A* **2010**, *527*, 2738–2746. [CrossRef]

30. Krauss, G. *Steels: Processing, Structure, and Performance*, 2nd ed.; ASM International: Materials Park, OH, USA, 2015; pp. 335–369.

31. Wei, R.; Enomoto, M.; Hadian, R.; Zurob, H.S.; Purdy, G.R. Growth of austenite from as-quenched martensite during intercritical annealing in an Fe-0.1C-3Mn-1.5Si alloy. *Acta Mater.* **2013**, *61*, 697–707. [CrossRef]

32. Yuan, S.; Xie, Z.; Wang, J.; Zhu, L.; Yan, L.; Shang, C.; Misra, R.D.K. Effect of heterogeneous microstructure on refining austenite grain size in low alloy heavy-gage plate. *Metals* **2020**, *10*, 132. [CrossRef]

33. Li, X.; Li, C.; Cao, N.; Lin, X.; Sun, J. Crystallography of reverted austenite in the intercritically reheated coarse-grained heat-affected zone of high strength pipeline steel. *Acta Metall. Sin.* **2021**, *57*, 967–976. [CrossRef]

34. Kocks, U.F.; Mecking, H. Physics and phenomenology of strain hardening: The FCC case. *Prog. Mater Sci.* **2003**, *48*, 171–273. [CrossRef]

35. Ghassemi-Armaki, H.; Maaß, R.; Bhat, S.P.; Sriram, S.; Greer, J.R.; Kumar, K.S. Deformation response of ferrite and martensite in a dual-phase steel. *Acta Mater.* **2014**, *62*, 197–211. [CrossRef]

36. Balliger, N.K.; Gladman, T. Work hardening of dual-phase steels. *Met. Sci.* **1981**, *15*, 95–108. [CrossRef]

37. Pierman, A.P.; Bouaziz, O.; Pardoen, T.; Jacques, P.J.; Brassart, L. The influence of microstructure and composition on the plastic behaviour of dual-phase steels. *Acta Mater.* **2014**, *73*, 298–311. [CrossRef]

38. Li, X.D.; Fan, Y.R.; Ma, X.P.; Subramanian, S.V.; Shang, C.J. Influence of martensite–austenite constituents formed at different intercritical temperatures on toughness. *Mater. Des.* **2015**, *67*, 457–463. [CrossRef]

39. Li, X.D.; Shang, C.J.; Ma, X.P.; Gault, B.; Subramanian, S.V.; Sun, J.B.; Misra, R.D.K. Elemental distribution in the martensite–austenite constituent in intercritically reheated coarse-grained heat-affected zone of a high-strength pipeline steel. *Scripta Mater.* **2017**, *139*, 67–70. [CrossRef]

40. Gourgues, A.F. Electron backscatter diffraction and cracking. *Mater. Sci. Technol.* **2002**, *18*, 119–133. [CrossRef]